ELSEVIER

Available online at www.sciencedirect.com

SCIENCE DIRECT®

Nuclear Instruments and Methods in Physics Research B 222 (2004) 667–680

NIM B Beam Interactions with Materials & Atoms

www.elsevier.com/locate/nimb

Apparatus for real time in situ quantitative studies of growing nanoparticles by grazing incidence small angle X-ray scattering and surface differential reflectance spectroscopy

G. Renaud *, M. Ducruet, O. Ulrich, R. Lazzari [1]

Département de Recherche Fondamentale sur la Matière Condensée/SP2M/NRS, CEA Grenoble, 17, rue des Martyrs, Grenoble Cedex 9, 38054, France

Received 6 February 2004; received in revised form 18 March 2004

Abstract

This paper describes an experimental setup that was developed to simultaneously perform grazing incidence small angle X-ray scattering (GISAXS) and surface differential reflectance spectroscopy (SDRS) measurements in ultra-high vacuum, in situ, during the three-dimensional growth of islands on a substrate, from the very beginning of the growth up to coalescence in the film. Four major features of this new GISAXS setup are: (i) the absence of window between the X-ray source and the sample, thus avoiding any unwanted background scattering; (ii) the use of a high grade two-dimensional CCD detector; (iii) very high flux from an ESRF undulator beamline; (iv) the ability to subtract the reference from the bare substrate before deposit. This results in two-dimensional measurements that are background-free and extend over a very large intensity dynamic of a few 10^4. This allows for the first time to perform measurements on very small deposits (as low as 0.01 nm of equivalent thickness) and to record measurements in real time without interrupting the growth process. Two softwares have been developed and can be freely downloaded from the WEB in order to perform a very detailed quantitative analysis of the both GISAXS and SDRS data, allowing to probe the island size and separation from 1 to ~50 nm.
© 2004 Elsevier B.V. All rights reserved.

PACS: 61.10; 07.85.−n; 81.10.−h; 68.35.−p
Keywords: GISAXS; In situ; Morphology; Nano-particles; Self-organized growth; Buried dislocation network

1. Introduction

Islands of nanometric size deposited on a substrate might have fascinating new properties, which are of interest both for basic and applied research. For instance, nanometer-sized metallic islands spread on ceramic substrates may have enhanced surface chemical reactivity and thus useful catalytic properties [1]; islands of magnetic metal may be magnetic-monodomain and have original spin-dependent transport properties [2]; or small, coherently strained semiconductor islands called "quantum dots" may have remarkable opto-electronic properties [3]. Novel device applications could result from such systems, provided a

* Corresponding author. Tel.: +33-4-3878-3558; fax: +33-4-3878-5138.
E-mail address: grenaud@cea.fr (G. Renaud).
[1] Now at Groupe de Physique des Solides, CNRS UMR 7588 – Universités Paris VI–VII, Campus de Boucicaut, 140 rue de Lourmel, 75015 Paris, France.

0168-583X/$ - see front matter © 2004 Elsevier B.V. All rights reserved.
doi:10.1016/j.nimb.2004.04.158

large number of similar islands could be grown. In all cases, the properties of these nanostructures depend to a great extent on their shape, size, size distributions and ordering, which in turn depend on the growth conditions. It is therefore essential to characterise these quantities precisely as a function of the growth parameters such as substrate quality, temperature and deposition rate. From a more fundamental point of view, the growth processes themselves, which are governed by a competition between kinetics and thermodynamics, are very important to investigate, in order to deduce the energy barriers involved and the influence of the substrate-induced stress. Near-field imaging techniques, such as atomic force microscopy (AFM) and scanning tunnelling microscopy (STM) or transmission electron microscopy (TEM) are routinely used to characterise the island morphology but have some limitations, such as limited statistics, convolution with the tip shape, difficulty to use on bulk insulating substrates and to use in situ during growth. X-ray scattering is a choice method to complement these techniques and to overcome their limitations. It is adapted to any kind of sample, conducting or not; it can be used in any kind of sample environment and in all pressure and temperature ranges. It can also be used *in real time* during a reaction or during growth. X-ray scattering directly provides statistical information on size distributions and ordering by macroscopically sampling the growing film, thus giving an image of the "mean island". In addition, varying the incidence of the X-ray beam gives different depth sensitivities, from the very surface to deeply buried interfaces, enabling to probe the morphology of embedded clusters.

In this article, we describe an apparatus that was especially developed to measure in situ the morphology of growing islands on a substrate [4], as a function of growth parameters (time and substrate temperature), in ultra-high vacuum (UHV), from the beginning of growth up to the later stages (several tens of nanometres), by two techniques used simultaneously: grazing incidence small angle X-ray scattering (GISAXS) [5–8] and surface differential reflectivity spectroscopy (SDRS). The principle of GISAXS is first recalled, before the experimental setup is presented and next detailed as well as the complementary SDRS technique. We finally illustrate the potential of the two techniques on three cases: (i) the growth of Ag on MgO(0 0 1) because it is representative of the 3D growth of many metals on oxide surfaces and is a model system to investigate the elementary processes of heterogeneous catalysis and silver/oxide is a test bed for optical techniques; (ii) the self-organised growth of Co on the Au(1 1 1) surface is chosen as an example of self-organised growth; and (iii) the case of substrates having a buried interfacial network of misfit dislocations.

2. Principle of GISAXS

The principle of GISAXS is shown in Fig. 1: a narrow and well collimated incident X-ray beam, of wavevector $\mathbf{k}_i$ (modulus $k = 2\pi/\lambda$) impinges on the surface at a grazing angle α_i, of the order of the critical angle for total external reflection. The scattered intensity is measured on a 2D detector as a function of the in-plane and out-of plane scattering angles 2θ and α_f, which are related to the momentum transfer co-ordinates as

$$q_x = k(\cos\alpha_f \cos 2\theta - \cos\alpha_i);$$
$$q_y = k(\cos\alpha_f \sin 2\theta - \cos\alpha_i);$$
$$q_z = k(\sin\alpha_f + \sin\alpha_i).$$

At small angles (a few degrees), the curvature of the Ewald's sphere can be, most of the time, neglected ($q_x \sim 0$) and the reciprocal space scales

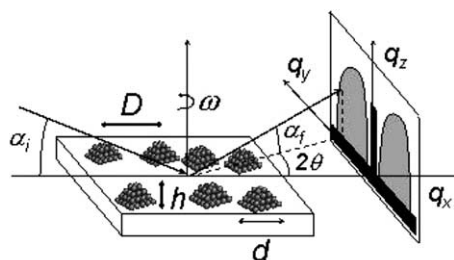

Fig. 1. Principle of GISAXS: an incoming X-ray beam illuminates the sample surface under grazing α_i angle; the signal is collected at small angles $(2\theta, \alpha_f)$ on the detector plane. The sample can be rotated around its surface normal.

with the co-ordinates $q_y k \sim \sin 2\theta$ and $q_z \sim k(\sin\alpha_f + \sin\alpha_i)$, respectively parallel and perpendicular to the surface. The intensity is measured very close to the origin of the reciprocal space, and hence $q_{y,z}$ span a small range, of a few per inverse nanometres. If nanometer-size inhomogeneities of the electron density such as islands, roughness or electronic contrast variation are present on the surface, they scatter the incident, reflected and transmitted beams in a way that depends on their morphology and topography [9]. The sample can be rotated around its surface normal by an ω rotation, defining the orientation of the incident X-ray beam with respect to the in-plane crystallographic directions, which is necessary to investigate anisotropic islands. A T-shape beam-stop absorbs the direct and reflected beam before they hit the detector.

3. Experimental setup

Because the signal is very close to the direct beam, a major constraint in GISAXS (like in usual bulk small angle X-ray scattering) is to decrease as much as possible the background arising from the beam divergence, from all the optical elements of the beamline, and from windows placed in the beam path. This requires a bright beam with a very low divergence, high quality optical elements and several pairs of slits to define the beam and remove unwanted low-angle scattering. More importantly, when performing surface X-ray scattering in ultra-high vacuum (UHV) to study molecular beam epitaxy growth (MBE), a beryllium window is usually present on the sample chamber to keep the UHV while letting the X-ray beam entering and exiting the chamber. This also implies a Be window at the end of the beamline as well as some path of the X-ray beam travelling in air between the beamline and the chamber. These Be windows and air-path generate large background scattering at small angle, which in addition varies very quickly with small, micrometric variations (which are inevitable on a synchrotron beamline) of the beam impact on the Be window. To avoid these sources of background, we have chosen to hook directly the chamber to the beamline, and to avoid any window between the sample and the X-ray source. The only Be window is at the end of the beam path, just before the 2D detector; it does not provide any additional background as the unwanted diffuse signal is hidden by the beam stop before it diverges. This choice of all vacuum setup implied developing dedicated slits, monitor and beam shutter, as well as installing several differentially pumped pipes to connect parts with different base vacuum levels. Fig. 2 shows a schematic drawing of the experimental setup, whose different parts are described below. Figs. 3

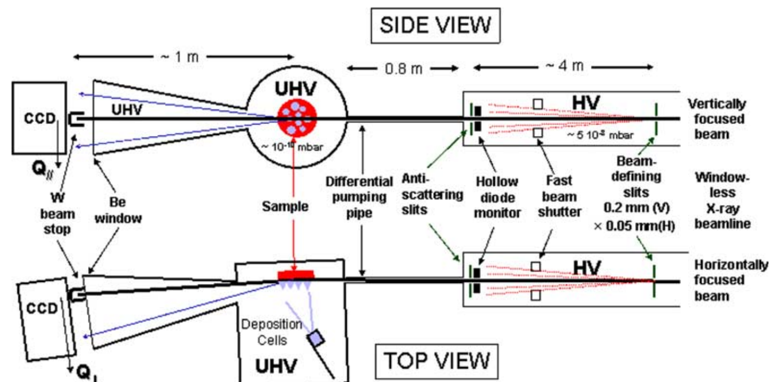

Fig. 2. Schematic drawing of the experimental setup located in the experimental X-ray hutch. All the beam path between the X-ray source and the sample is in high or ultra-high vacuum, with no scattering element such as Be window in between, thus avoiding the usual small angle scattering background due to windows.

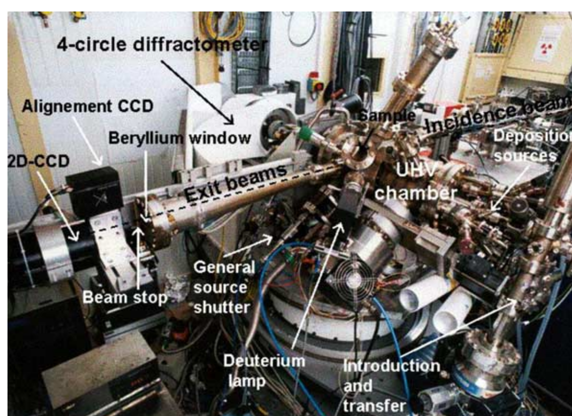

Fig. 3. Photograph of the experimental setup viewed from the end of the experimental hutch. The X-ray beam enters from the right; the sample is vertical, in the centre of the UVH chamber.

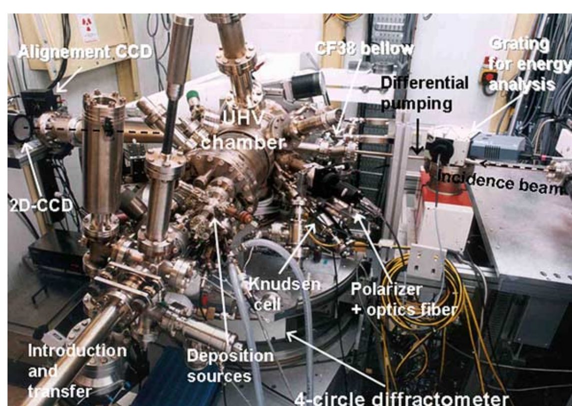

Fig. 4. Photograph of the experimental setup viewed from the sample transfer line. The X-ray beam enters from the right. The grating spectrograph and the output optical table for surface differential reflectance measurements are visible.

and 4 show photographs of the main parts of the setup.

4. Beamline setup

The X-ray beam was delivered by two undulators of 48 and 40 mm period inserted in a high β straight section of the European Synchrotron Radiation facility (ESRF-Beamline ID32) at Grenoble, France [10]. They provide photons from about 2.5 keV up to more than 40 keV. The entire beamline is windowless, connected to the UHV of the storage ring via differentially pumped sections and delay lines backed by fast valves. The first optical element was a double-crystal monochromator: a first silicon (1 1 1) crystal, cryogenically cooled in order to cope with the full power-load of the source, and a second, independent monochromator crystal providing sagittal focusing of the beam to the end stations [11]. The second optical element of the beamline consisted of a 450 mm long mirror based on bimorph technology. This mirror provided vertical focussing and harmonic rejection.

The optimized beamline setup resulted in a beam size before slits of 0.5×0.2 mm^2 ($H \times V$) FWHM (full width at half maximum) and a beam divergence of 2×10^{-5} (H) and 4×10^{-6} rad (V) FWHM, with a flux larger than 10^{12} photons/s. Two pairs of motorized slits working in high vacuum were developed and installed respectively 5 and 1 m upstream the sample. The first pair of slits was used to define the beam size (0.05 mm $H \times 0.2$ mm V), and the second pair was used to remove the scattering by the primary slits. These slits were originally standard HUBER 3013. The two pairs of independent slits were separated, inserted in a UHV cross with four CF100 and two CF38 tubes connected to the CF38 beamline on both ends (Fig. 5(a)). Two CF100 were connected to pumps, the two other being used to motorise the slits thanks to

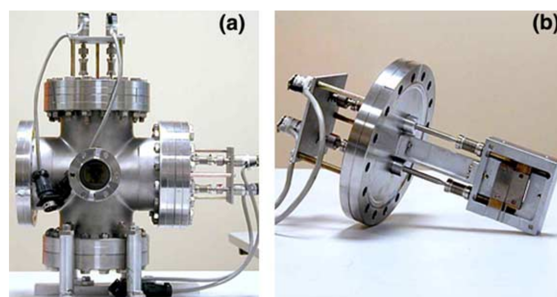

Fig. 5. (a) UHV cross containing a pair of HUBER 3013 slits adapted to vacuum and motorized from the outside. Each cross is pumped by a 60 l/s Varian Starcell ion pump connected to the bottom flange, and a 80 l/s turbomolecular pump connected on the left flange. (b) Detailed view of mounting of the HUBER slits and rotary feedthrough on a flange.

a small stepping motor and a rotary feedthrough for each blade (Fig. 5(b)). A fast (∼5 ms of closure time) beam shutter (XRS6 from Uniblitz) was uncapped and cooled down by a large copper holder, and installed in a dedicated UHV cross just before the secondary slits (Fig. 5). Finally, a hollow diode was mounted in vacuum just before the secondary slits, in order to monitor the beam intensity by measuring the beam vertically scattered by the primary slits. Several CF38 valves with 10 mm diameter Be windows at the centre were installed at different locations along this 6 m long beamline, together with several bellows to allow for alignment of the different parts with the beam. This setup was aligned by dedicated manual vertical and horizontal translations. All this beam-defining assembly was pumped by several ion and turbomolecular pumps, enabling to reach a vacuum of $\sim 5\times 10^{-8}$ mbar. A 0.8-m long, 8 mm inner diameter differential pumping pipe pumped by a large ion pump, and allowing a differential pressure of more than four orders of magnitude between both ends, was installed between this beam-defining line and the UHV chamber (base pressure 10^{-10} mbar) mounted on a diffractometer.

5. Diffractometer

The six circle diffractometer of "2 + 2" type [12] has been described in detail elsewhere [13]. We only recall here the main characteristics. The detector has two rotary motions around a vertical and a horizontal axis, respectively. The sample has one rotation around a vertical axis, defining the incident angle α_i with respect to the vertical surface, and an azimuthal rotation ω around a horizontal axis. Three jacks (0.3 μm resolution) mounted on air pads allow levelling and adjustment of the goniometer height. The whole diffractometer can slide laterally perpendicular to the beam thanks to three air pads and a horizontal motorized translation. A remarkable feature of this goniometer is its high accuracy, even for large and heavy sample environments (up to 200 kg): all rotation axes intersect to within 15 μm; all rotations have absolute accuracy of 0.01° or better, and repeatability better than 0.001°. The actual position is known to within 0.0005° thanks to Heidenham ROD 800 and LIDA 360 absolute encoders. The different axes have been aligned either parallel or perpendicular to within 0.001°.

6. UHV chamber

This chamber; which is visible on the two photographs (Figs. 3 and 4) is a modification of that described in [13]: the beryllium window and low energy electron diffraction parts have been replaced by parts with many more flanges, most of them visible on the photographs. Different surface preparation tools were available: Ar^+ ion bombardment, furnace, or heating under O_2 partial pressure (up to 5×10^{-4} mbar). The chamber was equipped with up to five evaporation sources: two MECA-2000 evaporation Knudsen cells and three Omicron EFM4 electron-beam evaporators. Deposition of Ag, Pd, Pt, Au, Co, Ge and Si have been performed, with deposition rates between 0.001 and 0.1 nm/min, as in situ calibrated by a quartz microbalance. Remote controlled shutters were available on the different evaporators, as well a general one in front of the sample. All UHV tools could be used without moving the sample from its X-ray scattering position, thus avoiding time consuming realignments, and allowing in situ experiments. The samples could be inserted into a load-lock system pumped down to $\sim 1\times 10^{-8}$ mbar before they were transferred in the X-ray chamber thanks to a magnetic transfer rod. They were held by a custom made horizontal axis manipulator holding a high temperature furnace especially developed by Meca-2000, which allows heating radiatively up to 850 °C and up to 1400 °C by electron bombardment. The one-inch Molyblock sample holders are held on the furnace without any motion thanks to a ring connected to three springs pushing at the back of the sample holder. The sample manipulator is directly connected to, and held by, the goniometric ω 360° rotation with horizontal axis. The transmission of this ω rotation inside the chamber is realized thanks to a commercial (Thermoionics RNN600) differentially pumped rotary feedthrough linked with a welded bellows. As described in detail in [13], three precise

motorized motions are brought into UHV by the manipulator: a horizontal translation with 0.1 μm resolution and two perpendicular tilts of 0.001° resolution and ±3° range. They respectively allow to bring the sample surface at the goniometer centre, and to precisely align the surface normal with the ω axis. Two viewports are located on opposite sides of the chamber, to allow the prealignment of the surface using a laser beam, and pyrometric measurement of the sample's temperature.

The beam enters the UHV chamber by a CF38 tube hooked to the entrance line thanks to a CF38 bellows, allowing for a small rotation of the chamber around the vertical axis, used to define the angle of incidence of the X-ray beam with respect to the surface of the sample. A 260 l/s Varian turbomolecular pump, a Meca-2000 water-cooled titanium sublimation pump and a 120 l/s Starcell Varian ion pump lying below the chamber, inside the large goniometer α-circle, allows a vacuum of $\sim 10^{-10}$ mbar to be maintained during MBE deposition, X-ray data acquisition and low-temperature (up to 600 °C) heating. Above 600 °C, long annealings induce pressure rises in the 10^{-9} mbar range. A quadrupole mass analyzer was also available to control the residual gases.

At the opposite side from the incoming beam, a 0.8-m long cone was connected to an exit pipe through a CF38 bellow, and ended by a 100 mm diameter beryllium window (Fig. 6) placed in front of a X-ray two-dimensional detector, thus avoiding small angle scattering background. The cone and the detector were hooked to the goniometer detector arm, allowing for precise vertical and horizontal alignment. A motorized tungsten beam-stop with a T-shape was introduced between the exit Be window and the 2D detector (Fig. 6(b) and (c)) to hide the direct and reflected beams. Several beam stops with different sizes were precisely machined by electro-erosion. They had a central slot to avoid scattered beams reaching the detector, into which a tungsten wire could be inserted to measure the intensity inside the beam stop through the generated photoelectric current. The wire was insulated everywhere except at the location of the reflected beam, thus providing a monitor of the beam effectively reaching the sample. It was found well correlated with the primary monitor (hollow diodes), although this latter measured only a portion of the primary beam not reaching the sample. The detector was a 1242×1152 pixels 16 bits high grade (1 MPP) CCD from Princeton with a square acceptance of 65×65 mm and a threefold demagnification insured by a tapered assembly of optical fibres. The Phosphor screen of GdOS is optimized for energies between 3 and 30 keV. The full well capacity is 3×10^5 electrons, with a readout noise of 7 electrons (for 100 kHz reading). The CCD is cooled down to −60 °C by a four stages Peltier system, resulting in a very small dark current, below 0.02 electrons/pixel/s. The detector is under vacuum, and the X-rays enter through a 90 mm diameter 0.02-mm-thick Be window. It is mounted on the two-axis detector arm, at a variable distance (between 900 and 2000 mm) from the sample.

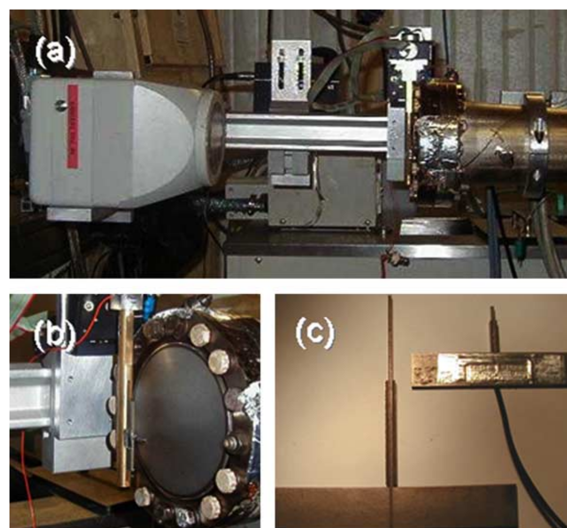

Fig. 6. (a) Photograph of the detection arm: 2D CCD detector (left) and end of vacuum chamber with Be window (right). (b) Close view of the Be window and the beam stop. (c) Two of the several T-shaped tungsten beam stops, including a wire used to monitor the beam.

7. Surface differential reflectance spectroscopy

7.1. Principle and sensitivity to morphology

An additional setup was added to perform surface differential reflectance spectroscopy (SDRS)

at the same time, in situ during growth. This technique, complementary to the GISAXS measurements, uses the photons in the UV–visible spectral range to probe, in a non-destructive way, the growth of nanoparticles. It has been intensively used in the past to study the fundamental dielectric properties of surfaces [14–16]. The probed quantity is the modification of the Fresnel reflectivity of the surface and thus of its dielectric properties upon deposition. In the case of the metal/oxide cluster growth, the signal arises from the so-called Mie absorption or plasmon resonances [17]. These latter are due to the polarisation of the metal electronic gas of the cluster upon the incident electric field and to the damping of the induced vibrating dipole. The key parameters are the cluster polarisabilities [17], which depend crucially on the particle shape through the depolarisation factor and on the image dipole inside the substrate. Moreover, the dipolar coupling between induced dipoles among the particle collection leads to a shift of the observed resonances, thus giving access to the particle density. The recorded signal is linearly proportional to the mean deposited thickness and is governed by the imaginary part of the cluster polarisabilities. The SDRS technique is well suited for free electron gas metals like alkaline or noble metals as silver, for which the lifetime of plasmon is long and its frequency belongs to the probed spectral range. Indeed, for transition metal, the plasmon resonances are broader because of inter-band transitions [17]. Moreover, charging effects of the insulating substrate are avoided with photon probe.

7.2. SDRS experimental setup

SDRS consists in measuring, as function of the radiation wavelength or energy (200–850 nm or 1.5–6 eV) the relative variation $\Delta R/R = (R - R_0)/R_0$ of the Fresnel reflection coefficient R during deposition, that of the bare substrate R_0 being used as a reference. Performing relative variation measurements allows to get rid of the unknown spectral transmittance of all the optical elements. The setup, which appears on the photographs of Figs. 3 and 4, is made of two compact optical tables mounted on two symmetrical CF38 flanges of the chamber, giving rise to an incident angle (taken from the surface normal) of 50°. The input and output flanges are equipped with silica viewports allowing the highest UV transmittance. The light emitted by a deuterium lamp (from Hamamatsu) is focused on the sample surface with a silica lens. The reflected light is polarised either in the plane of incidence (p-polarisation) or perpendicular (s-polarisation) with a large acceptance 1% extinction ultraviolet linear dichroic polarizer (transmission around 30%). The polarized signal is then focused thanks to an achromatic lens on the entrance of the circular end (25° acceptance) of a circular-to-rectangular fused silica fibre bundle. The other end forms the entrance slit (200 μm × 2.5 mm) of the spectrograph. This latter is an Oriel-MS 125 1/8 m compact grating monochromator equipped with a ruled 300 groves/mm grating (band pass 180–1000 nm). The grating is blazed at 300 nm to improve the UV efficiency; its position is setup with a micrometric screw thanks to the 657.3 nm intense emission line of deuterium. The wavelength dispersed light is collected on 1024, 2 mm × 25 μm, silicon photodiode array detection (PDA) system. PDA detector is preferred over CCD to achieve a high signal/noise ratio with a high saturation range. The PDA dynamical range is 1:40 000 and its quantum efficiency above 25% in all the spectral range of interest. The PDA is Peltier cooled down to −15 °C to reduce the dark noise; the read-out speed is chosen to be the slowest possible compared to the deposition kinetics to reduce the read-out noise. The main advantage of a spectrograph equipped with a PDA over a scanning monochromator with a punctual detector is the larger measurement speed. Accounting for all the optical path transmittance and of the low reflectivity of the oxide substrate studied, the exposure time needed to reach saturation can be reduced down to 0.2 s per spectrum. To improve statistics, each spectrum is made of several accumulations leading to a speed of roughly 5 s per spectrum. Pixel binning was unnecessary on the point of view of signal/noise ratio; owing to the broadness of the plasmon structure, the final spectral resolution of 1 nm is highly sufficient. The stability of the lamp and of the mechanical mounting allows reaching a

sensitivity of 0.5% on the differential signal. The use of a grating (compared to a prism) spectrograph on a wide spectral range implies a post-correction of second order diffraction, which was calibrated with a Hg(Ne) lamp with sharp optical transition lines. The sensitivity to 0.01 nm of metal equivalent thickness is linked to the strong dielectric contrast between metal and oxide and to the enhancement of the relative signal due to the small substrate reflectivity (a few % for MgO), particularly close to the Brewster angle (60° for MgO) in p-polarisation.

7.3. Data analysis

The data analysis and the underlying physical phenomena have been detailed elsewhere. For short, it is based on the concept of surface excess electromagnetic fields developed by Bedeaux and Vlieger during the last 30 years and recently reviewed in a book [18]. The Fresnel coefficients are expressed as function of surface susceptibilities which, in turn, depends on the polarisabilities of nanometric islands whose size is by far smaller than the optical wavelength. All the work consists in calculating such coefficients for fixed particle geometry. Simple shapes but realistic in term of wetting, like truncated sphere [19] or spheroids [20] have been fully treated; the polarisabilities are, in the quasi-static limit, computed through a multipolar expansion of the potential and the use of image charge technique. The matching of boundary conditions at different interfaces gives access to the desired coefficients. The dielectric properties of the media are taken equal to that of the bulk phases but with well known finite size corrections [20]. Despite the fact that the polarisation process is mainly of dipolar character, multipolar modes of vibration of the electric charges have non-zero oscillator strength [21,22]. It has been demonstrated [20] that (i) such a model is more accurate than the simplest Yamaguchi theory [23] and the thin plate models [24] and (ii) the experimental SDRS data can be reproduced with a good estimate of the morphological parameters in the case of clusters growth [20–22,24]. The developed simulation software are access free [25–27].

8. Experimental results

We illustrate the possibilities of the setup on three examples: the growth of Ag on an MgO(0 0 1) surface, the self-organized growth of Co on a "herringbone"-reconstructed Au(1 1 1) surface, and a buried two-dimensional dislocation network at a twisted Si(0 0 1)/Si(0 0 1) interface. In all cases, the GISAXS data have been corrected for the flat field and the dark without beam. In the first two cases, a reference GISAXS picture recorded on the bare substrate prior deposit has been subtracted.

8.1. Ag/MgO(1 0 0) Volmer–Weber growth

Fig. 7 shows a typical GISAXS picture obtained on a 2-nm-thick Ag deposit on MgO(0 0 1) at 500 K, with the incident X-ray beam parallel to the in-plane [1 1 0] direction of the substrate. Because of

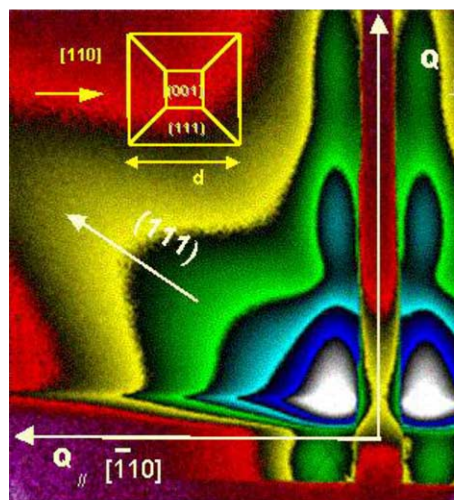

Fig. 7. A typical GISAXS picture recorded on a 2-nm-thick Ag deposit on a MgO(0 0 1) surface held at 500 K, in situ, in UHV, with the incident beam parallel to the substrate [1 1 0] direction. The X-ray wavelength was 0.12 nm, and the picture extends to 3 nm^{-1} in both directions. The vertical (respectively horizontal) direction is perpendicular (respectively parallel) to the sample surface. The direct beam is fully hidden by the beam stop, and the 1-mm-wide beam-stop extension perpendicular to the surface hides the reflected beam and specular reflectivity. The complete image was recorded in 0.4 s. The background is <1 count/pixel; the colour scale is logarithmic and the maximum intensity is 6×10^4 counts.

the small metal/oxide adhesion energy, the growth is three-dimensional (Volmer–Weber type), in the form of islands. The extension of the scattering parallel (respectively perpendicular) to the surface is inversely proportional to the lateral (respectively vertical) size of the islands. The absence of intensity minima parallel to the surface reveals a fairly wide distribution of lateral sizes. On the contrary, clear minima and maxima are observed perpendicular to the surface, showing that the distribution of islands heights is much narrower. Moreover, a rod of scattering oriented at 57° from the surface normal, and thus along the (1 1 1) direction, is visible. This rod arises from (1 1 1) planes in real space. These observations, together with additional measurements for different azimuthal orientations ω, point to an average shape based on a square pyramid exposing {1 1 1} facets, with the base edges parallel to the substrate ⟨1 1 0⟩ directions. The interferences perpendicular to the surface show that these pyramids have a flat (0 0 1) top facet: they are truncated. Parallel to the surface, two maxima in intensity, symmetrically placed with respect to the beam stop, are visible. They arise because the islands are not randomly distributed on the substrate, but are rather separated by a preferential nearest-neighbours (center-to-center) distance D (see Fig. 1). A remarkable feature is the very large extension of the intensity, over more than four orders of magnitude, and the negligible background, of the order of 1 count per pixel. This large dynamics and low background allow fully quantitative analysis of the data, with extraction of the island shapes and size distributions. Another new advantage of this setup is the very high intensity, which enabled to record these images in as low as 0.4 s. Even shorter exposure times can be used for larger deposits. The smallest deposit investigated had an equivalent thickness of 0.01 nm, and a few minutes of exposure were required to get good quality data. These characteristics allow recording GISAXS pictures during a complete growth, from the very beginnings up to percolation in the film (a few tenth of nanometres). For some deposits, we even recorded complete movies of the growth, with measurements in real time, thanks to small deposition rates (~0.001 nm/min). Fig. 8 shows GISAXS images obtained during the room-temperature growth of Ag on MgO(0 0 1) for some equivalent deposited thickness ranging from 0.1 to 10 nm. As growth proceeds, all characteristic features of the scattered intensity become more and

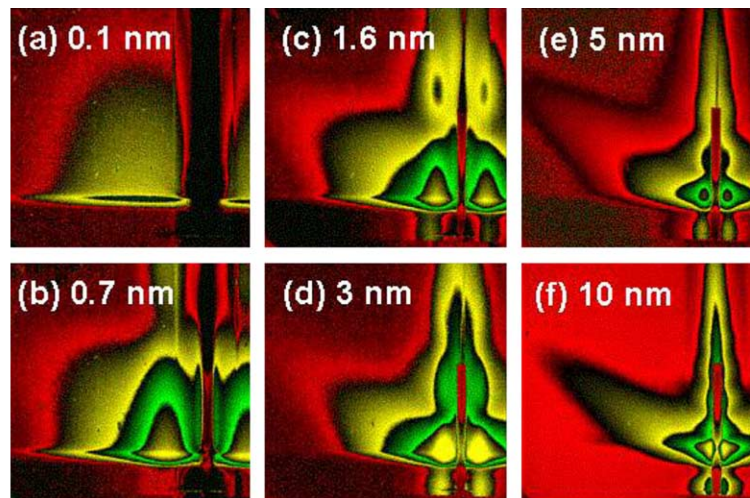

Fig. 8. Evolution of GISAXS images during the in situ growth, in UHV, of Ag on a MgO(0 0 1) surface at 300 K (wavelength 0.12 nm, extension up to 3 nm^{-1} in both directions). Six equivalent thicknesses are reported: 0.1 nm (a), 0.7 nm (b), 1.6 nm (c), 3 nm (d), 5 nm (e) and 10 nm (f). The thickness of the last deposit has been re-calibrated ex situ afterwards by Rutherford backscattering spectroscopy and X-ray microprobe. Each black contour between two colours corresponds to an order of magnitude change in intensity.

more concentrated toward the origin of reciprocal space, which reveals a classical nucleation, growth and coalescence of islands. Note the second order and even third order of scattering perpendicular to the surface, as well as the (1 1 1) rod, progressively appearing during growth. A web-available program called IsGISAXS has been developed for the analysis of these images, and is available as free download on the ESRF WEB site [9]. The detailed conclusions on these data will be reported elsewhere as done for the Pg/MgO(1 0 0) system [28]. The Ag/MgO(0 0 1) associated optical spectra are shown in Fig. 9. Two broad resonances are clearly visible. The low energy one, around 2.5 eV, is linked to the excited dipole parallel to the surface, and the high energy one, around 3.8 eV, corresponds to the plasmon resonance perpendicular to the substrate [20,21,25]. In between, a structure of quadrupolar character shows up because of the coupling between particles [22]. The analysis methodology of the optical response of islands has been described in the previous section. Fig. 10 shows the evolution with thickness of the average height h, lateral size d and separation D deduced

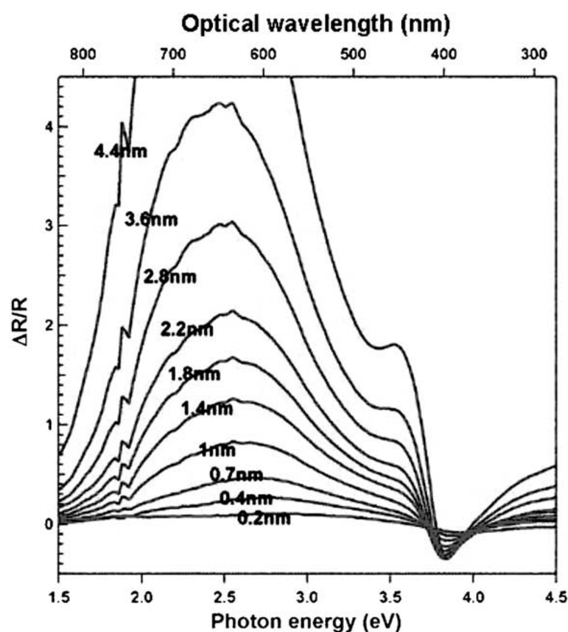

Fig. 9. SDRS optical spectra obtained during the same Ag deposition on MgO(0 0 1) substrate held at 300 K. The equivalent deposited thickness is given on each curve.

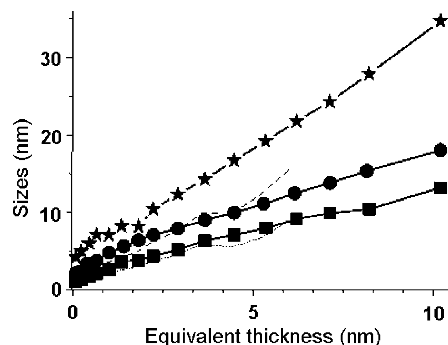

Fig. 10. Evolution with the equivalent thickness of the deposit, of the average height h (square), in-plane size d (disks) and separation D (stars), as deduced by a quantitative analysis of GISAXS measurements performed during the in situ growth of Ag on MgO(0 0 1) at 300 K. Also reported are the average height (dotted line) and lateral size (dashed line) as deduced from analysis of the simultaneous differential reflectance measurements.

from quantitative analysis of both methods for the 300 K growth data. These three sizes are observed to increase linearly with the deposited thickness. More importantly, these dimensional parameters deduced from the simultaneous measurements of GISAXS and SDRS, are in good agreement, showing the adequacy of both techniques to determine these cluster sizes, at least for this Ag/MgO case.

8.2. Self-organized growth of Co dots on the herringbone reconstruction of Au(1 1 1)

As a second example, Fig. 11 shows GISAXS pictures recorded during the self-organized growth of Co on the Au(1 1 1)($22\times\sqrt{3}$) reconstruction. Co is well known to form an ordered rectangular network of two atomic layer high islands [29] when deposited on the Au(1 1 1) herringbone reconstruction [30,31], with periods of 7.7 and ~17 nm respectively along the $[1\,1\,\bar{2}]$ and the $[1\,\bar{1}\,0]$ directions. The corresponding GISAXS pattern is a network of diffraction rods perpendicular to the surface, whose separation is inversely proportional to the periodicity in real space [32]. The island shape can not be accurately deduced from such data because all the information is concentrated in the scattering rods. In practice, only information on the repartition of the islands and degree of

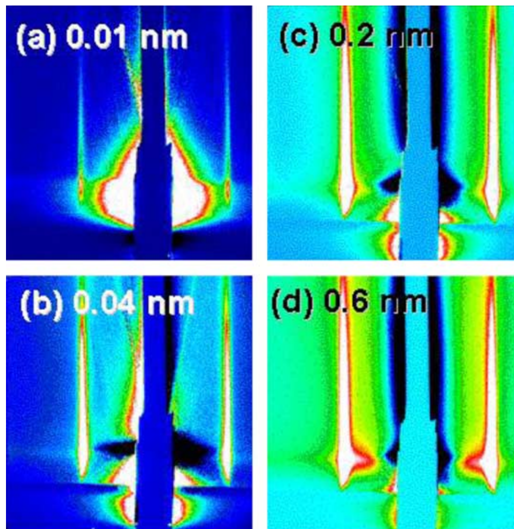

Fig. 11. Evolution of the GISAXS images (wavelength 0.12 nm, extension up to 2 nm^{-1} parallel to the surface, and 3 nm^{-1} perpendicular to it) during the in situ self-organized growth, in UHV, of Co dots on the "herringbone-reconstructed" Au(1 1 1) surface at room temperature, for four selected equivalent thicknesses of the deposit (0.01 nm (a), 0.04 nm (b), 0.2 nm (c) and 0.6 nm (d)). The vertical (respectively horizontal) direction is perpendicular (respectively parallel) to the sample surface. The direct beam is fully hidden by the beam stop, and the 3-mm-wide beam-stop extension perpendicular to the surface hides the reflected beam and specular reflectivity.

ordering could be deduced. The evolution as a function of Co thickness shows that the periodicity does not evolve during growth, only the intensity in the rods increases, corresponding to lateral growth of the Co islands already nucleated on the rectangular networks of elbows of the Au(1 1 1) surface. A first important point to note here is the sensitivity of GISAXS to very small amounts of deposited materials, as low as 0.01 nm. Most importantly, comparison with the Ag/MgO growth data shows the extreme sensitivity of GISAXS to organisation at the nanometre scale, whatever the internal structure (crystalline or not) of the scattering islands. This could be turned to account if searching for the proper kinetic conditions leading to self-organized growth. For standard "random" nucleation and growth, the intensity should be spread over a wide range parallel to the surface. A tendency toward organization of the clusters should be revealed by a progressive sharpening of the intensity parallel to the surface, transforming progressively into sharp rods for well ordered systems. This in general requires patterned substrates, such as those having an underlying network of dislocations emerging at the surface [33].

8.3. Surface nanopatterning by buried dislocations networks: molecular bonded silicon wafers

The last example concerns GISAXS by buried dislocation networks created at the interface between two molecularly bonded silicon wafers. The technique of molecular bonding of two identical silicon wafers with a very precise control of the misalignment in their crystallographic axis is described elsewhere [34]. Chosen twist angle ψ (Fig. 12(a)) and tilt angle θ (Fig. 12(b)) can be obtained, and the thickness h of the top silicon wafer can be rendered as small as 5 nm, thanks to the smart-cut technique [35] followed by polishing. Grazing incidence X-ray diffraction [36] and high resolution transmission electron microscopy measurements

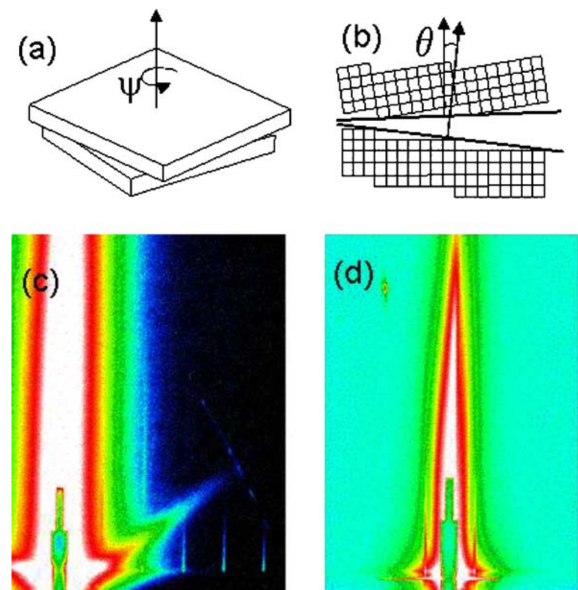

Fig. 12. Definitions of the twist ψ (a) and the tilt θ (b) angles for molecularly bonded silicon wafers. (c): GISAXS image recorded on a 10-nm-thick bonded Si layer for a pure twist bonding of 1°. (d) GISAXS image recorded on a 10-nm-thick bonded Si layer for a pure tilt. GISAXS was performed with a wavelength of 0.12 nm.

[37] showed that the twist results in a regular square interfacial network of screw dislocations of period d given by Frank's formula $d = a/(2\sqrt{2}\sin(\psi/2))$, where a is the silicon lattice parameter, while the flexion θ between the two crystals yields a periodic network of edge dislocations with a period $l = a/(2\sin\theta)$. These two networks induce a periodic strain field that propagates to the surface, through the top thin layer thickness h. The regular modulation of the electron density due to the in-plane rotation is extremely small, while that due to the tilt is two orders of magnitude larger. Both are in principle well accessible by wide angle X-ray scattering experiments [36], but should only yield an extremely small signal at small angles. Because of the intense beam in the present experiment, both modulations of the electron density were measurable in GISAXS, as shown in Fig. 12(c) and (d). The sample of Fig. 12(c) was molecularly bonded with a nominal twist $\psi = 1°$, and in such a way as to annihilate the miscut (by cutting the two silicon parts from the same original wafer, hence yielding the same miscut, and rotating in-plane the two wafers by 180° with respect to each other). Fig. 12(c) shows the GISAXS picture recorded with the beam aligned with the screw dislocation network (i.e. ~along the ⟨1 1 0⟩ direction). More than five rods of scattering extending perpendicular to the surface are measurable. These rods are very narrow in the direction parallel to the surface (with a full width at half maximum of 0.01824 nm^{-1}), which shows the very long-range ordering of the network, larger than 334 nm (because of the limited resolution). They are separated by an in-plane momentum transfer of 0.283 nm^{-1}, which corresponds to a 22.2 ± 0.3 nm periodicity in real space, and hence a twist of 0.995°, very close to the nominal one. One could ask whether this GISAXS signal arises from the strain field within the film, from the top surface corrugation or from both. Three observations indicate that the surface contribution is negligible. The first is that STM measurements where performed on similar samples, and never revealed a surface modulation (provided the samples are not acid etched); the second is that more than five orders of diffraction are measured, while a top surface corrugation would likely be close to a sine function [38], thus yielding significant intensity only in the very first orders of scattering parallel to the surface. Last but not least, the rods are observed to decrease quickly as a function of the perpendicular momentum transfer, showing that they arise from an object having a significant thickness. A surface corrugation would yield rods extending much farther perpendicular to the surface. Note the wide rod of scattering making an angle of 57° with respect to the surface normal, and hence extending along the (1 1 1) direction. This presumably arises from stacking faults along the (1 1 1) planes, due to partial dissociation of the dislocations. Hence this measurement shows that even the extremely weak small angle scattering signal from screw dislocations can be measured.

Another sample was prepared, with the in-plane crystallographic axes perfectly parallel (i.e. with nominally zero twist), but with a tilt estimated to be ~0.45°. GISAXS measurements were performed as a function of the in-plane orientation of the incident X-ray beam with respect to the in-plane crystallographic axes. Well defined rods of scattering perpendicular to the surface were again observed (Fig. 12(d)) with a fourfold symmetry, but with only the first diffraction order being sizeable, in contrast with the previous measurement, showing they have a different origin. They correspond to a real-space periodicity of 35.5 nm. Based on the hypothesis that they arise from the square misfit dislocation network generated but the tilt, a tilt value of $\theta = 0.437°$ is obtained, again in good agreement with the nominal value. Note that the intensity is more than one order of magnitude larger than that due to twist dislocations, as expected since the induced displacement field is much larger. The double intensity line parallel to the surface can be explained by multiple scattering events, which are described elsewhere [9].

This last example demonstrates that GISAXS can also be used to probe buried interfaces, as well as the top surface.

9. Conclusion and perspectives

In conclusion, we have developed a new setup to perform combined grazing incidence small angle

X-ray scattering and surface differential reflectance spectroscopy measurements in situ, in UHV, during Volmer–Weber growth of islands on a substrate, and sometimes in real time. The combination of high brightness, grazing incidence, very low background and all-UHV in situ studies yields two-dimensional GISAXS measurements with a very high signal-to-noise ratio. This yields high sensitivity, allowing quantitative analysis with extraction of shape, sizes and size distributions as a function of growth, even for very small deposited thickness ~0.01 nm. The island size or separation can range from ~1 to ~50 nm. The data are extremely sensitive to the degree of ordering, so that the technique could be very helpful to determine the best conditions for self-organized growth, in a much shorter time than with STM or AFM, with the additional advantage that a macroscopic area of the sample is probed. "Real time" measurements as a function of deposition or annealing time are possible since the acquisition time is very small (typically a minute for 0.01 nm thickness and 0.1 s for 1 nm). This kind of measurements could be very important for the growth of embedded islands, since GISAXS is the only in situ non-destructive structural technique that can probe deep into a layer. The potential of the method is wide, since measurements can be performed for instance at high pressure, high temperature, during the course of a catalytic reaction, or in growth reactors, by chemical vapour deposition or sputtering techniques. In the future, this technique could be combined with grazing incidence X-ray scattering at large angle [39], thus simultaneously probing the atomic structure (epitaxial relationships, misfit relaxation, coherent or incoherent, etc.) inside the islands and their morphology. In addition, magnetic morphological or structural information could also be obtained in principle by performing measurements at several wavelengths near the adsorption edge of element [40].

Acknowledgements

We would like to acknowledge all the ID32 ESRF staff for there helps to setup these experiments, especially Pascal Bernard. J. Eymery and F. Leroy are also thanked for the bonded silicon measurements; O. Fruchart, A. Barbier, J.P. Deville, F. Scheurer for the Co/Au(1 1 1) measurements, and J. Jupille and Y. Borensztein for the Ag/MgO(0 0 1) ones.

References

[1] M. Valden, X. Lai, D.W. Goodman, Science 281 (1998) 1647.
[2] K. Wildberger, V.S. Stepanyuk, P. Lang, R. Zeller, P.H. Dederichs, Phys. Rev. Lett. 75 (1995) 509.
[3] For a review, see e.g.Mater. Res. Soc. Bull. 23 (1998).
[4] G. Renaud, R. Lazzari, C. Revenant, A. Barbier, M. Noblet, O. Ulrich, F. Leroy, J. Jupille, Y. Borensztein, C.R. Henry, J.P. Deville, F. Scheurer, J. Mane-Mane, O. Fruchart, Science 300 (2003) 1416.
[5] J.R. Levine, J.B. Cohen, Y.W. Chung, P. Georgopoulos, J. Appl. Cryst. 22 (1989) 528.
[6] J. Stangl, V. Holy, T. Roch, A. Daniel, G. Bauer, J. Zhu, K. Brunner, G. Abstreiter, Phys. Rev. B 62 (2000) 7229.
[7] D. Babonneau, A. Naudon, D. Thiaudière, S. Lequien, J. Appl. Cryst. 32 (1999) 226.
[8] M. Schmidbauer, Th. Wiebach, H. Raidt, M. Hanke, R. Köhler, H. Wawra, Phys. Rev. B 58 (1998) 10523.
[9] R. Lazzari, J. Appl. Cryst. 35 (2002) 406, http://www.esrf.fr/computing/scientific/joint_projects/IsGISAXS/.
[10] http://www.esrf.fr/.
[11] F. Comin, Rev. Sci. Instr. 66 (1995) 2082.
[12] K.-W. Evans-Lutterodt, Tang-Mautsu, J. Appl. Cryst. 28 (1995) 318.
[13] G. Renaud, B. Villette, P. Guénard, Nucl. Inst. and Meth. B 95 (1995) 422.
[14] Y. Borensztein, Surf. Rev. Lett. 7 (2000) 399.
[15] P. Chiaradia, R. Del Sole, Surf. Rev. Lett. 6 (1999) 517.
[16] D.S. Martin, P. Weightman, Surf. Rev. Lett. 7 (2000) 389.
[17] U. Kreibig, M. Vollmer, Optical Properties of Metal Clusters, Springer Verlag, Berlin, 1995.
[18] D. Bedeaux, J. Vlieger, Optical Properties of Surfaces, Imperial College Press, London, 2001, and references therein.
[19] I. Simonsen, R. Lazzari, J. Jupille, S. Roux, Phys. Rev. B 61 (2000) 7722.
[20] R. Lazzari, I. Simonsen, D. Bedeaux, J. Vlieger, J. Jupille, Eur. Phys. J. B 24 (2001) 267.
[21] R. Lazzari, S. Roux, I. Simonsen, J. Jupille, D. Bedeaux, J. Vlieger, Phys. Rev. B 65 (2002) 235424-1.
[22] R. Lazzari, I. Simonsen, J. Jupille, Europhys. Lett. 61 (2003) 541.
[23] T. Yamaguchi, S. Yoshida, A. Kinbara, Thin Solid Films 18 (1973) 63;
T. Yamaguchi, S. Yoshida, A. Kinbara, Thin Solid Films 21 (1) (1974) 173.

[24] J.D. McIntyre, D.E. Aspnes, Surf. Sci. 24 (1971) 417.
[25] R. Lazzari, J. Jupille, Appl. Surf. Sci. 142 (1999) 451; R. Lazzari, J. Jupille, Surf. Sci. 482–485 (2001) 823.
[26] R. Lazzari, I. Simonsen, Thin Solids Films 419 (2002) 124.
[27] http://www.phys.ntnu.no/~ingves/Software/GranularFilm/.
[28] C. Revenant, F. Leroy, R. Lazzari, G. Renaud, C.R. Henry, Phys. Rev. B 69 (2004) 035411.
[29] B. Voigtländer, G. Meyer, N.M. Amer, Phys. Rev. B 44 (1991) 10354.
[30] J. Barth, H. Brune, G. Ertl, R. Behm, Phys. Rev. B 42 (1990) 9307.
[31] A.R. Sandy, S.G.J. Mochrie, D.M. Zehner, K.G. Huang, D. Gibbs, Phys. Rev. B 43 (1991) 4667.
[32] O. Fruchart, G. Renaud, A. Barbier, M. Noblet, O. Ulrich, J.P. Deville, F. Scheurer, J. Mane-Mane, V. Repain, G. Baudot, S. Rousset, Europhys. Lett. 63 (2003) 275.
[33] A. Bourret, Surf. Sci. 432 (1999) 37.
[34] D. Buttard, J. Eymery, F. Fournel, P. Gentille, F. Leroy, N. Magnea, H. Moriceau, G. Renaud, F. Rieutord, K. Rousseau, J.-L. Rouvière, IEEE J. Quant. Elect. 38 (2002) 995.
[35] F. Fournel, K. Rousseau, H. Moriceau, J. Eymery, J.L. Rouvière, N. Magnéa, B. Aspar, Appl. Phys. Lett. 80 (2002) 793.
[36] J. Eymery, D. Buttard, F. Fournel, H. Moriceau, G.T. Baumbach, D. Lûbbert, Phys. Rev. B 65 (2002) 165337.
[37] K. Rousseau, J.L. Rouvière, F. Fournel, H. Moriceau, Appl. Phys. Lett. 80 (2002) 4121.
[38] F. Leroy, J. Eymery, D. Buttard, G. Renaud, R. Lazzari, F. Fournel, Appl. Phys. Lett. 82 (2003) 2598.
[39] G. Renaud, Surf. Sci. Rep. 32 (1998) 1.
[40] H.A. Dürr, E. Dudzik, S.S. Dhesi, J.B. Goedkoop, G. Van der Laan, M. Belakhovsky, C. Mocuta, A. Marty, Y. Samson, Science 284 (1999) 2166.